*Short Communication*

# Preparation and Electrochemical Performance of Mg-doped Li$_4$Ti$_5$O$_{12}$ Nanoparticles as Anode Materials for Lithium-Ion Batteries

*Fuyun Li, Min Zeng*[*]*, Jing Li, Hui Xu*

School of Materials Science and Engineering, Southwest University of Science and Technology, Mianyang 621010, P R China
[*]E-mail: zengmin@swust.edu.cn

Mg-doped Li$_4$Ti$_5$O$_{12}$ nanoparticles with a grain size of around 200 nm were synthesized successfully using a simple solid-state reaction route. The effects of Mg$^{2+}$ doping on Li$_4$Ti$_5$O$_{12}$ were systematically investigated by XRD, XPS, TEM, HRTEM and EDS. These indicated that Mg ions were uniformly dispersed into Li$_4$Ti$_5$O$_{12}$ lattice and Mg$^{2+}$ doping during sintering can effectively inhibit the growth of Mg-doped Li$_4$Ti$_5$O$_{12}$ particles without changing the structure of Li$_4$Ti$_5$O$_{12}$. The charge–discharge cycling tests and EIS analysis were conducted to study their electrochemical performance. The initial discharge capacity of the Mg-doped Li$_4$Ti$_5$O$_{12}$ electrodes was 190mAhg$^{-1}$ at 1 C and the discharge capcity of 179mAhg$^{-1}$ was retained after 100 cycles. Moreover, the discharge capacity of 150mAhg$^{-1}$ was maintained even at a high rate of 5 C after 100 cycles, whereas the undoped electrodes only exhibited a capacity of 134mAhg$^{-1}$ under the same condition. The excellent electrochemical performance of doped electrodes can be ascribed to the unique properties of nanomaterials and excellent electrical conductivity due to Mg$^{2+}$ doping.

## 1. INTRODUCTION

As power sources, lithium-ion batteries (LIBs) have been intensively used for portable electronic devices (e.g. cellphones) owing to their outstanding properties such as relatively high energy density, long lifespan, low self-discharge, light weight and ambient temperature operation, and so on [1-3]. With the growing demands for large-scale energy storage applications, it is a crucial issue to develop long life LIBs with high energy and power density [4-7]. A titanium oxide electrode material, Li$_4$Ti$_5$O$_{12}$, is a promising alternative anode materials for LIBs as a result of its several advantages

(good Li-ion intercalation and deintercalation reversibility, excellent Li-ion mobility and no structural change during charge–discharge process) [8-10]. However, the poor electrical conductivity ($\sigma < 10^{-13}$ S cm$^{-1}$) and the sluggish lithium ion diffusion coefficient ($<10^{-8}$ cm$^2$ s$^{-1}$) of $Li_4Ti_5O_{12}$ greatly limit its rate performance [2, 11]. To improve the electrical conductivity of $Li_4Ti_5O_{12}$, many effective methods have been proposed, including synthesis of nanosized $Li_4Ti_5O_{12}$ [12-13], doping with conductive metal ions ($Zn^{2+}$, $Cr^{3+}$, $Ni^{2+}$, $Mg^{2+}$) [14-17] or non-metal ions ($F^-$) [18] in Li, Ti or O sites, and coating conductive materials on $Li_4Ti_5O_{12}$, such as carbon coating layer [19-20], N-Doped Carbon coating layer [21] and $TiO_2$ nano-coating layer and so on [22].

Based on the merits mentioned above, we considered if the synthesis of nanosized $Li_4Ti_5O_{12}$ with $Mg^{2+}$ doping can further improve the electrochemical performances of $Li_4Ti_5O_{12}$, as the so-called "Synergistic Effect". It should be noted that the ionic radius of $Mg^{2+}$ (0.66 Å) was nearly the same as that of $Li^+$ (0.68 Å), and Mg ions were easily incorporated into the Li sites. In this work, nanosized $Li_4Ti_5O_{12}$ with $Mg^{2+}$ doping was prepared by a cheap method of the nanosized raw materials. The effects of nanosized materials and $Mg^{2+}$ doping on the electrochemical performances of $Li_4Ti_5O_{12}$ have been studied at ambient temperatures.

## 2. EXPERIMENTAL

### 2.1. Preparation of $Li_4Ti_5O_{12}$ and Mg-doped $Li_4Ti_5O_{12}$

The $Li_4Ti_5O_{12}$ (LTO) and Mg-doped $Li_4Ti_5O_{12}$ (Mg-LTO) samples were synthesized by a solid state reaction. The starting materials were powers of $Li_2CO_3$ (AR, Chengdu kelong Chemical Agents Co. Ltd), nanosized $TiO_2$ (P25, Degussa) and MgO (99.9%, 50nm, Aladdin Co.). The raw materials were dissolved in ethanol slurry according to the stoichiometric quantities of $Li_4Ti_5O_{12}$ and $Li_{3.8}Mg_{0.2}Ti_5O_{12}$. About 8 wt% excess $Li_2CO_3$ was added to compensate for Li volatilization during the calcination process. Next, the mixture was ball-milling for 6 h and then the slurry was dried at 80 °C for 8 h. After being absolutely dried, the mixture was calcined at 800 °C for 8 h in air.

### 2.2. Characterizations and testing

The samples were initially characterised by X-ray diffraction using an X-ray diffraction analyzer with Cu-Kα radiation (X´Pert PRO, PANalytical). The surface chemical composition and the oxidation valence states of both samples were measured on an X-ray photoelectron spectroscopy (XPS), using a Perkin-Elmer model PHI 5600 XPS system. The more detailed structural information was measured on a transmission electron microscope (TEM) and a high-resolution transmission electron microscope (HRTEM, Tecnai F20, FEI). The morphology and doped element distribution of Mg-LTO were investigated by means of field emission scanning electron microscope (Ultr55, Zeiss) .

The electrochemical characterizations were realized in CR2016-type coin cell. The working electrodes were fabricated by mixing the active materials, super P and polyvinylidene difluoride (PVDF) in a weight ratio of 80:10:10, and then milled homogeneously in an agate mortar.

Subsequently, an appropriate amount of N-methylpyrrolidone (NMP) solvent was slowly introduced and wetly mixed to produce electrode slurry. The uniform slurry was coated onto a copper foil using a scraper and dried at 120 °C for 24 h to remove the solvent. Then the electrodes were punched into disks and assembled into half cells in an Ar-filled glove box. Li foils were used as the counter electrodes and the polypropylene microporous films (Celgard 2300) were employed as the separators. The commercial electrolyte was 1 M solution of $LiPF_6$ in ethylene carbonate (EC) and dimethyl carbonate (DMC) with in a volume ratio of 1:1. The charge–discharge measurement at room temperature was carried out using a LAND test system with cut-off voltage of 1.0–2.5 V (*vs.* $Li/Li^+$) at various constant current densities (1–5 C). Electrochemical impedance spectroscopy (EIS) was measured by means of a CHI760C electrochemical station in the frequency range of 0.01 Hz to 10 kHz.

## 3. RESULTS AND DISCUSSION

X-ray diffraction patterns of the pristine LTO and Mg-LTO are presented in Fig. 1(a). The diffraction peaks of both samples were sharp and strong, suggesting their high crystallinity. The diffraction patterns of LTO with and without MgO are in good agreement with cubic spinel LTO (JCPDS 49-0207). Moreover, the ionic radius of $Mg^{2+}$ (0.66 Å) was nearly the same as that of $Li^+$ (0.68 Å), and hence Mg ions were easily incorporated into the Li sites [3]. No secondary peaks belonging to MgO were detected in the XRD patterns of Mg-LTO in Fig. 1(a), which indicated that the doped Mg ions might be introduced into Li sites in the LTO lattice without changing its structural characteristics.

The surface chemical composition and the oxidation valence states of LTO and Mg-LTO were examined by X-ray photoelectron spectroscopy (XPS) measurement, as shown in Fig. 1(b-d). The XPS survey spectra of LTO and Mg-LTO are shown in Fig. 1(b). A new peak at around 310 eV for the Mg-LTO can be seen clearly, which can belong to Mg (KLL), indicating the presence of Mg in the surface of Mg-LTO. Fig. 1(c) and (d) show the typical high-resolution XPS spectra of Ti 2p for LTO and Mg-LTO, respectively. Two broad peaks at about 463.8 and 458.1 eV correspond well with characteristic Ti $2p_{1/2}$ and Ti $2p_{3/2}$ peaks of $Ti^{4+}$ in Fig. 1(c) [3, 10]. It can be clearly seen that almost all of the peak areas are attributed to $Ti^{4+}$ and only a tiny peak area assigns to $Ti^{3+}$ with a content of 3.68%. However, the curve of Ti 2p in Mg-LTO has a blue shift when compared to LTO. This indicates that treatment with $Mg^{2+}$ doping changed the surface bonding of LTO. Moreover, it can be seen that the contents of $Ti^{3+}$ at $2p_{3/2}$ and $2p_{1/2}$ in Fig. 1(d) are 15.68% and 17.23%, respectively, which are much higher than the content in LTO. This implies that $Ti^{4+}$ may be partially reduced to $Ti^{3+}$. On the basis of the results of Rietveld refinement and XPS analysis, $Mg^{2+}$ must have been doped into both the tetrahedral 8a Li sites and the octahedral 16d Li/Ti sites of LTO. This result is consistent with the XRD results (Fig. 1(a)). The above discussion indicate that $Mg^{2+}$ doping into Li sites can promote the reduction of $Ti^{4+}$ to $Ti^{3+}$ to balance the charge. It was reported that the $Ti^{3+}$ ions in LTO can effectively improve the concentration of electron–hole [17]; therefore, a larger proportion of $Ti^{3+}$ can effectively improve bulk electrical conductivity. In consequence, Mg-LTO would exhibit preferable electrical conductivity.
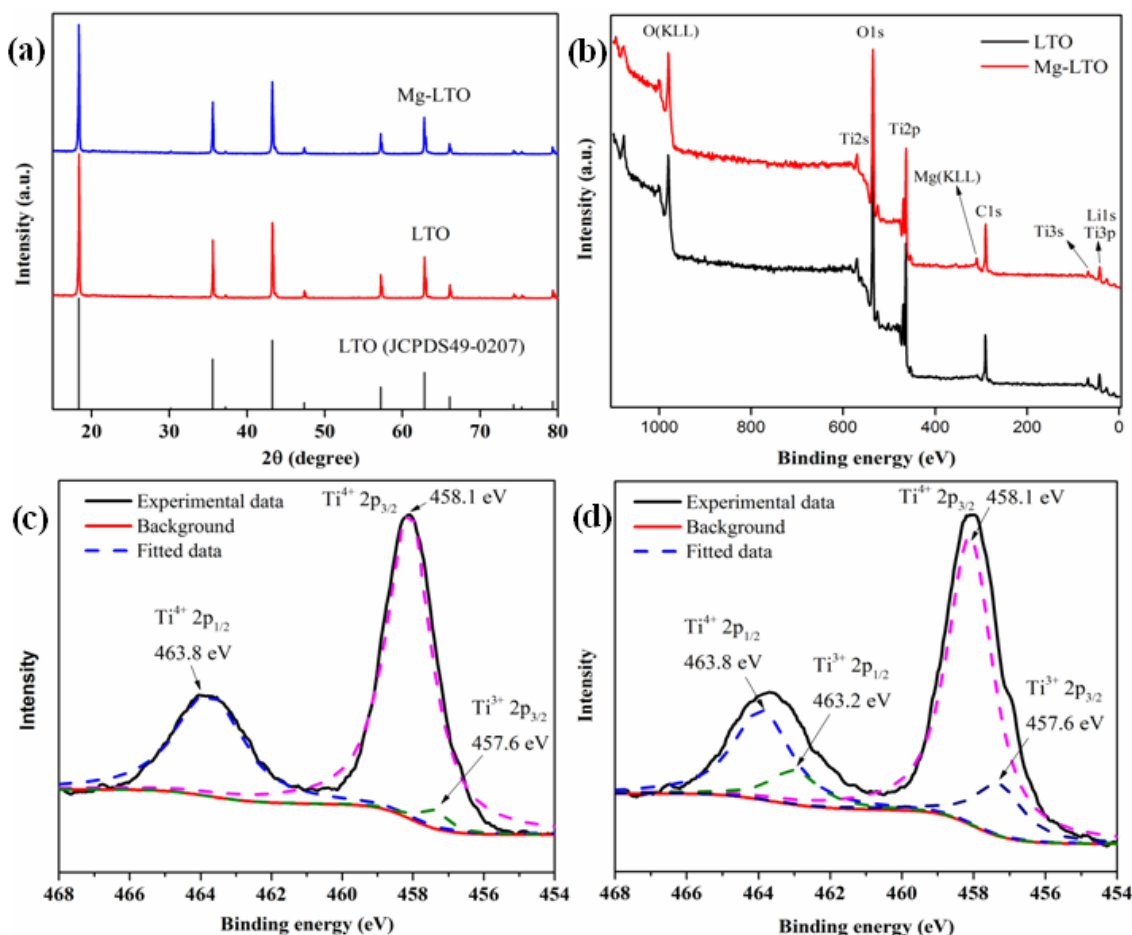
**Figure 1.** (a) XRD images of LTO and Mg-LTO. (b) XPS survey spectra of LTO and Mg-LTO. $Ti_{2p}$ XPS spectra of (c) LTO and (d) Mg-LTO.

The TEM micrographs and SEAD images of LTO and Mg-LTO are observed in Fig. 2(a) and (b). Compared with the LTO shown in Fig. 2(a), Mg-LTO (Fig. 2(b)) had smaller grain size around 200 nm, indicating that $Mg^{2+}$ doping during sintering can effectively inhibit the growth of Mg-LTO particles. Small size will make grains contact with electrolyte more sufficiently, and hence enhance the electrochemical property of the electrode. The insets in the images show selected area electron diffraction (SAED) images of the as-synthesized products. The regular distribution of sharp spots reveals that the LTO and Mg-LTO samples are monocrystal materials with a good crystal structure.

The HRTEM patterns (Fig. 2(c) and (d)) of LTO and Mg-LTO show that the structure of both samples is well crystallized. As shown in Fig. 2(c), the interplanar spacing of pristine LTO is 4.832 Å, which is well consistent with the lattice space (111) facets of spinel LTO [22]. However, the (111) facet of the Mg-LTO sample is ca. 4.653 Å (Fig. 2(d)), which is a bit smaller than the pristine LTO. This can be due to substitution of $Mg^{2+}$ for $Li^+$. The ionic radius of $Mg^{2+}$ and $Li^+$ is similar, but the electrovalence of $Mg^{2+}$ is twice that of $Li^+$. Thus, the ionic bonding interactions between $Mg^{2+}$ and $[TiO_6]$ octahedrons are stronger than that between $Li^+$ and $[TiO_6]$ octahedrons, which decreases the interplanar spacing.

To investigate the distribution of elements in doped sample, the elemental mapping of Mg-LTO was analyzed using Energy Dispersion Spectroscopy (EDS) measurement. As presented in Fig. 3, the

bright spots correspond to the presence of the elements Ti and Mg, which demonstrates that the Ti and Mg is uniformly distributed in the Mg-LTO crystal structure by means of the high temperature solid-stated reaction. This result reveals that the $Mg^{2+}$ may be introduced into Li sites in the LTO instead of separated phase.
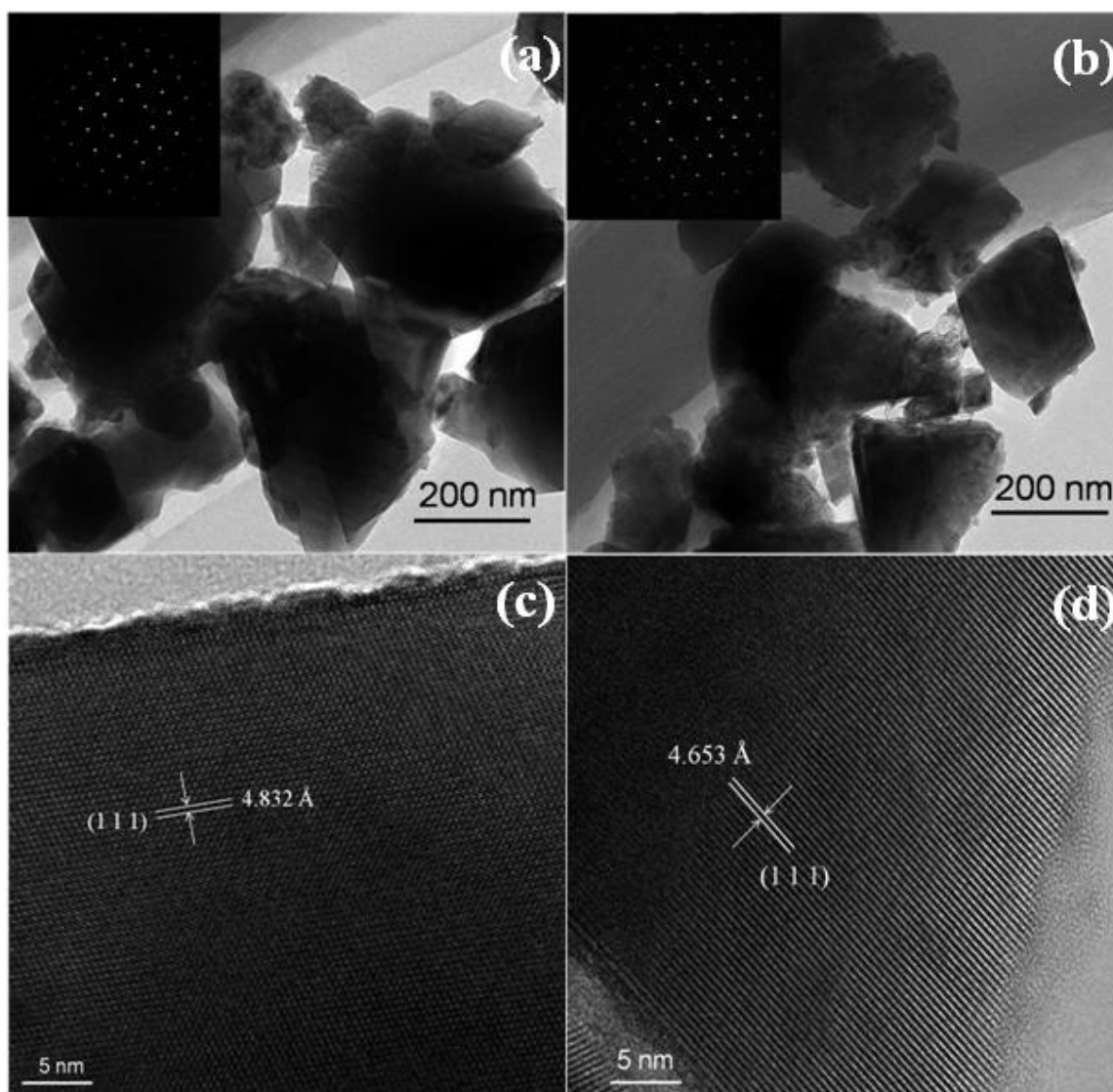


**Figure 2.** TEM micrographs and corresponding SEAD images (insets) of (a) LTO and (b) Mg-LTO. HRTEM patterns of (c) LTO and (d) Mg-LTO.

The electrochemical performance of LTO and Mg-LTO was evaluated at different charge–discharge rates from 1 to 5 C (Fig. 4). Fig. 4(a) and (b) show the initial cycle of typical (dis)charge profiles of LTO and Mg-LTO at different current rates. The Mg-LTO displayed the first discharge capacities of 191, 180, and 174 mAh $g^{-1}$ at rates of 1, 2 and 5 C, respectively. However, the LTO delivered the first discharge capacities of 177, 158, and 140 mAh $g^{-1}$ at rates of 1, 2 and 5 C, respectively. It is important to note that the first discharge specific capacity of the Mg-LTO samples is a higher than that of LTO at different rates. Moreover, the decrease in capacity with the increase in

current densities is an innate material response, but the difference in discharge capacities of two electrodes was magnified with the increase in the rate shown in Fig. 4(c) (e.g., 14 mAh g$^{-1}$ at 1 C, 22 mAh g$^{-1}$ at 2 C and 34 mAh g$^{-1}$ at 5 C). The discussion mentioned above indicates that Mg$^{2+}$ doping can effectively improve the performance of LTO at high rate.
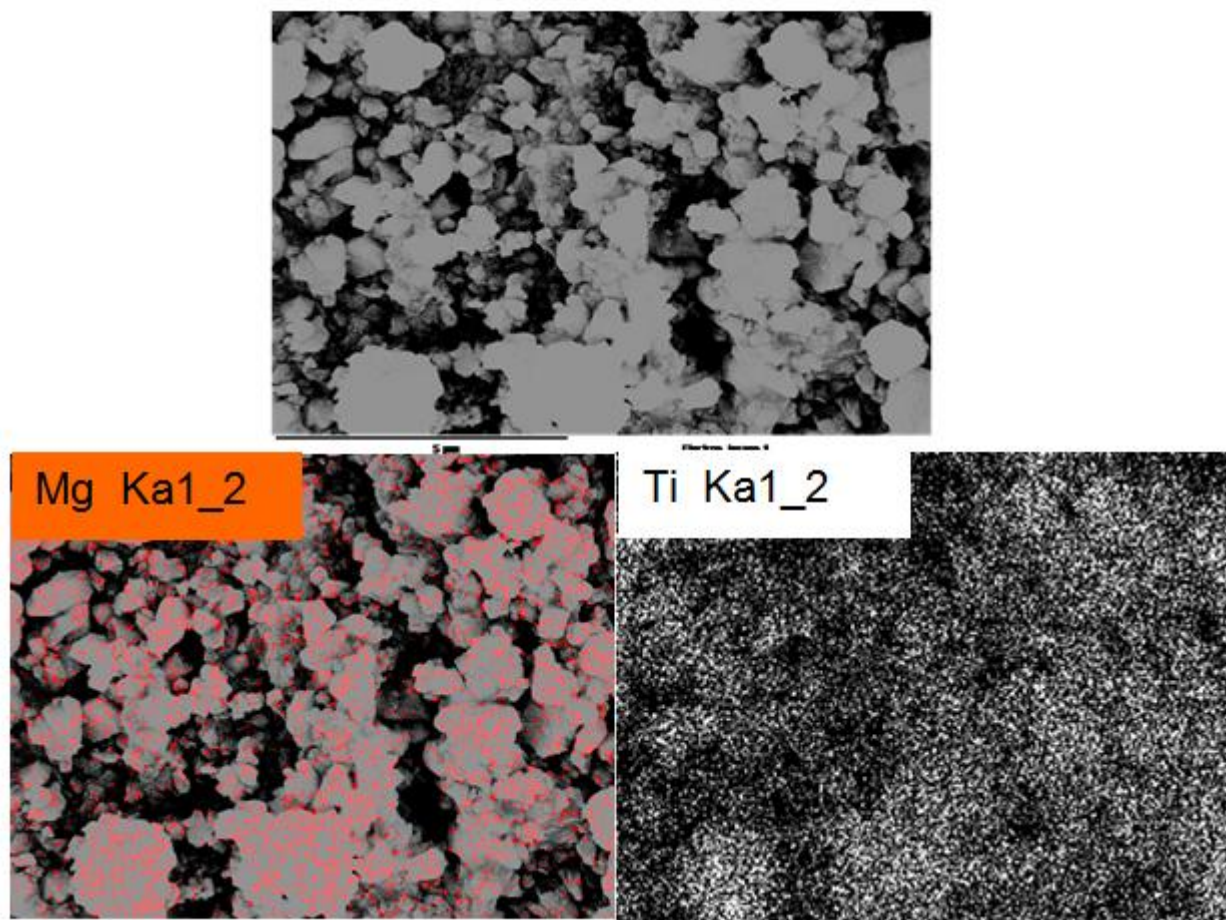


**Figure 3.** SEM image and the corresponding elemental mapping of Mg and Ti in the Mg-LTO.

The flat plateau position of the charge and discharge curves for both samples at about 1.7 and 1.5 V can be ascribed to the redox reactions of Ti$^{4+}$/Ti$^{3+}$ in LTO. The charge curve moves to higher potential and the discharge curve moves to lower potential with increasing of the charge–discharge current densities, which is due to the polarization of the electrode. Moreover, the charge–discharge voltage plateaus of the Mg-LTO are slightly closer to the theoretical voltage plateau (1.55 V) than the pristine LTO. This result demonstrates that, with the increase of the current densities, the Mg-LTO displays a smaller electrode polarization than the pristine LTO; manifesting that Mg$^{2+}$ doping can enhance the electrode reaction kinetics.

In order to examine the cycling performance of the LTO and Mg-LTO, the cyclic response at various rates for 100 cycles was conducted. As shown in Fig. 4(d), both electrodes, whether LTO or Mg-LTO, display good cycling stability at different rates from 1 to 5 C for 100 cycles. The discharge capacity of Mg-LTO was kept at 178.1 mAh g$^{-1}$ after 100 cycles at 1 C. Even after 100 cycles at 5 C, it

still displayed a discharge capacity of 150 mAh g$^{-1}$. On the basis of previous results, the higher-than-theoretical capacity could be attributed to the possible occupation at the 8a sites of nanosized LTO by Li$^+$ when the 16c sites of the spinel structure exceed the storage limit [23]. The co-occupation of 8a and 16c sites in the surface region is predicted to be more momentous in nanosized materials that have larger specific surface area, leading to storage properties of surface region different from those of the bulk [24]. In addition, Mg-LTO exhibits higher rate capability than LTO electrodes at different rates. For instance, Mg-LTO offers a capacity of about 165mAhg$^{-1}$, while LTO only displays an inferior capacity of 150 mAh g$^{-1}$ at 2 C rate after 100 cycles. Two complementary aspects clearly account for this considerable rate capability improvement (relative to LTO): (1) Compared with the pristine LTO, Mg-LTO had smaller grain size around 200 nm, and small size will make grains contact with electrolyte more sufficiently. (2) Mg$^{2+}$ doping may promote the electrical conductivity of Mg-LTO. These factors result in significant improvement of the electrode kinetics, and hence the specific capacity of Mg-LTO electrode is larger than that of LTO electrode.
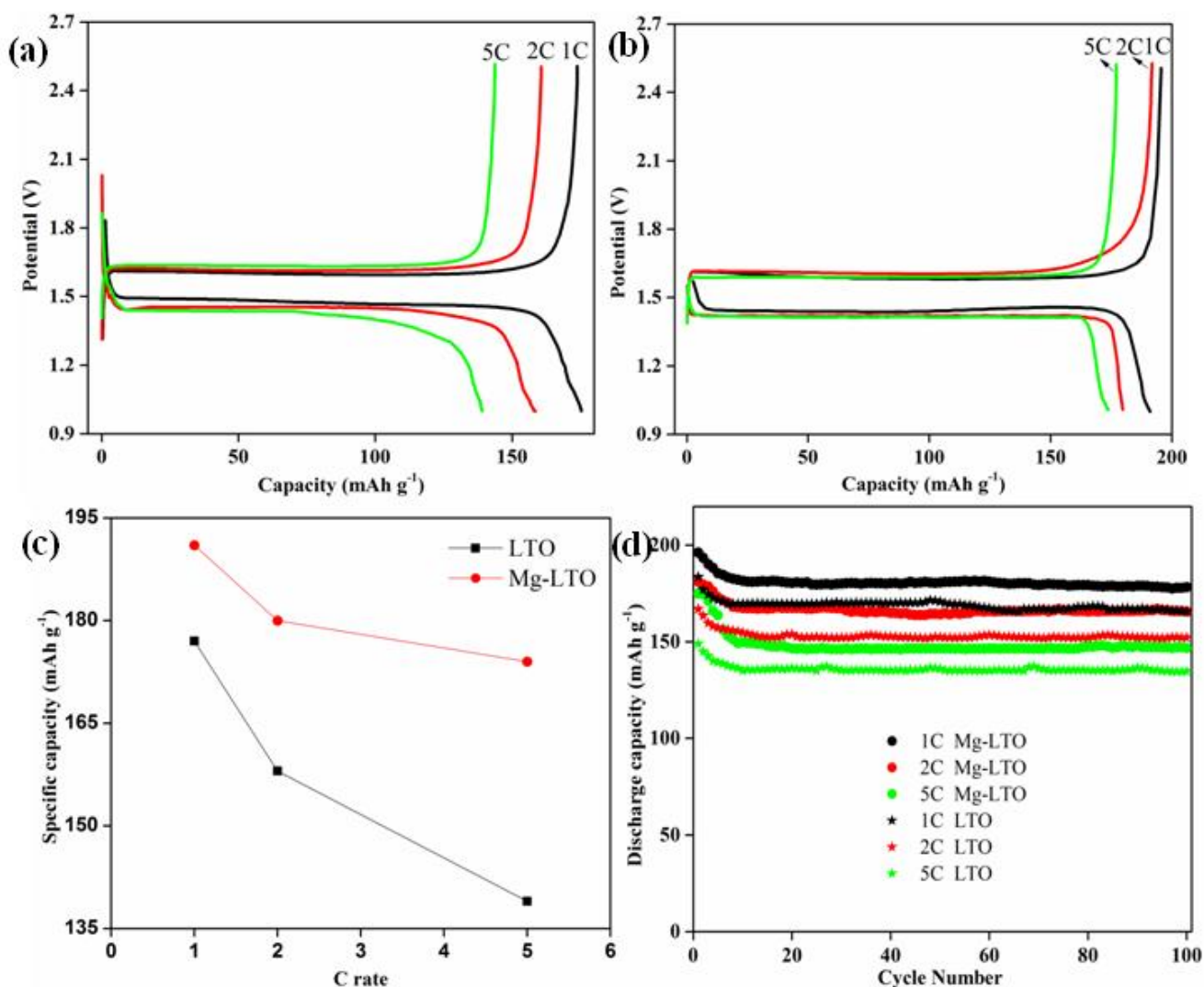


**Figure 4.** The initial charge–discharge curves for (a) LTO and (b) Mg-LTO at 1 C/1 C-5 C rates. (c) Dependence of specific capacity on C rate for LTO and Mg-LTO. (d) Cycling performance of the LTO and Mg-LTO powders.

To further gain insight into the reason of improved performance of Mg-LTO, electrochemical impedance spectroscopy (EIS) measurements were conducted (Fig. 5). The resulting Nyquist plots show a depressed semicircle in the high frequency region, and an inclined straight line in the low frequency region. The semicircular arc of the Mg-LTO electrode was smaller compared with the LTO electrode. The relatively small semicircular arc displays an overall smaller charge transfer resistance at the electrode/electrolyte interface after $Mg^{2+}$ doping. The inclined line in the low-frequency region is corresponded to $Li^+$ diffusion in the bulk of the material [18]. The Mg-LTO electrode displayed a larger slope, which may be used to imply a higher $Li^+$ mobility in the solid than the LTO. This result agrees with the electrochemical testing results (Fig. 4).
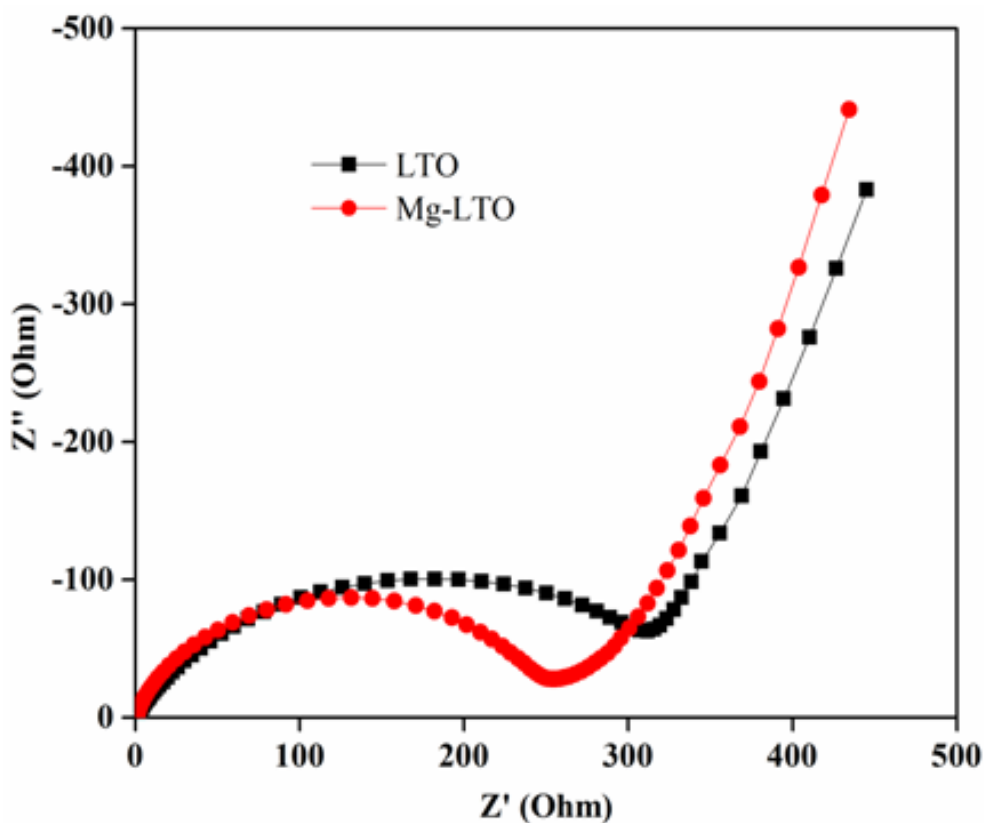


**Figure 5.** Nyquist impedance spectra of LTO and Mg-LTO materials.

## 4. CONCLUSIONS

In conclusion, nanoparticles LTO and Mg-LTO were successfully synthesized using a cheap method. We have studied the doping mechanism and the effects of $Mg^{2+}$ doping on the crystal structure, morphology, and electrochemical performance of LTO. Mg-LTO displays superior rate performance and cycling stability due to a larger specific surface area and lower resistance. Even after 100 cycles at 5 C, it still delivered a discharge capacity of 150 mAh g$^{-1}$. As a result, the Mg-LTO electrodes derived from the proposed solid-state reaction method can be considered as a promising anode material for high-performance LIBs.

**References**

1.  Y. C. Yang, B. H. Qiao, X. M. Yang, L. B. Fang, C. C. Pan, W. X. Song, H. S. Hou and X. B. Ji, *Adv. Funct. Mater.*, 24 (2014) 4349.
2.  S. Chen, Y. L. Xin, Y. Y. Zhou, Y. R. Ma, H. H. Zhou and L. M. Qi, *Energ Environ. Sci.*, 7 (2014) 1924.
3.  D. Z. Kong, W. N. Ren, Y. S. Luo, Y. P. Yang and C. W. Cheng, *J. Mater. Chem*. A, 2 (2014) 20221.
4.  L. F. Shen, E. Uchaker, X. G. Zhang and G. Z. Cao, *Adv. Mater.*, 24 (2012) 6502.
5.  K. Song, D. H. Seo, M. R. Jo, Y. Kim, K. Kang and Y. M. Kang, *J. Phys. Chem. Lett.*, 5 (2014) 1368.
6.  E. Kang, Y. S. Jung, G. H. Kim, J. Y. Chun, U. Wiesner, A. C. Dillon, J. K. Kim and J. Lee, *Adv. Funct. Mater.*, 21 (2011) 4349.
7.  Q. Y. Zhang and X. Li, *Int. J. Electrochem. Sci.*, 8 (2013) 7816.
8.  C. C. Yang, H. C. Hu, S. J. Lin and W. C. Chien, *J. Power Sources*, 258 (2014) 424.
9.  M. D. Ji, Y. L. Xu, Z. Zhao, H. Zhang, D. Liu, C. J. Zhao, X. Z. Qian and C. H. Zhao, *J. Power Sources,* 263 (2014) 296.
10. C. C. Chen, Y. N. Huang, C. H. An, H. Zhang, Y. J. Wang, L. F. Jiao and H. T. Yuan, *ChemSusChem*, 8 (2015) 114.
11. C. F. Lin, B. Ding, Y. L. Xin, F. Q. Cheng, M. O. Lai, L. Lu and H. H. Zhou, *J. Power Sources*, 248 (2014) 1034.
12. E. Pohjalainen, T. Rauhala, M. Valkeapää, J. Kallioinen and T. Kallio, *J. Phys. Chem. C,* 119 (2015) 2277.
13. L. F. Shen , X. G. Zhang , E. Uchaker , C. Z. Yuan and G. Z. Cao, *Adv. Energy Mater.*, 2 (2012) 691.
14. T. Zhou, Y. B. Lin, G. Y. Zhao, Y. D. Huang, H. Lai, J. X. Li, Z. G. Huang and S. H. Wu, *Int. J. Electrochem. Sci.*, 8 (2013) 1316.
15. S. Y. Li, M. Chen, Y. Xue, J. Wu, X. G. Zhang and Z. B. Wang, *Ionics*, 21 (2015) 1545.
16. C. C. Zhang, D. Shao, Q. Z. Gao, Y. H. Lu, Z. T. Liu, X. Y. Yu, Y. P. Fang and D. Y. Chen, *J. Phys. Chem.* C, 119 (2015) 2277.
17. W. Wang, B. Jiang, W. Y. Xiong, Z. Wang and S. Q. Jiao, *Electrochim. Acta*, 114 (2013) 198.
18. Y. Ma, B. Ding, G. Ji and J. Y. Lee, *ACS Nano,* 7 (2013) 10870.
19. Y. C. Kuo and J. Y. Lin, *Electrochim. Acta*, 142 (2014) 43.
20. C. G. Nava-Dino, R. G. Bautista-Margulis, J. E. Mendoza-Negrete, G. Llerar-Meza, J. P. Flores de los Rios, G. López-Ocaña, M. I. Ferrer-Sánchez, J. G Chacón-Nava and A. Martínez-Villafañe, *Int. J. Electrochem. Sci.*, 10 (2015) 3820.
21. L. Zhao, Y. S. Hu, H. Li, Z. X. Wang and L. Q, Chen. *Adv. Mater.*, 23 (2011) 1385.
22. Y. Q. Wang, L. Gu, Y. G. Guo, H. Li, X. Q. He, S. Tsukimoto, Y. C. Ikuhara and L. J. Wan, *J. Am. Chem. Soc.,* 34 (2012) 7874.
23. W. J. H. Borghols, M. Wagemaker, U. Lafont, E. M. Kelder and F. M. Mulder, *J. Am. Chem. Soc.*, 131 (2009) 17786.
24. Z. Zhong, C. Ouyang, S. Shi and M. Lei, *ChemPhysChem*, 9 (2008) 2104.